Inhibitory efficacy and structural insights of Bofutrelvir against SARS-CoV-2 Mpro mutants and MERS-CoV Mpro

Check for updates

Weiwei Wang [1,5], Xuelan Zhou[2,5], Wenwen Li[2], Pei Zeng[3], Li Guo[4], Qisheng Wang [1,6] ✉ & Jian Li [2,6] ✉

The COVID-19 pandemic has caused significant global health and economic disruption. Mutations E166N, E166R, E166N, S144A and His163A in the SARS-CoV-2 main protease (Mpro) have been implicated in reducing the efficacy of certain antiviral treatments. Bofutrelvir, a promising inhibitor, has shown effectiveness against SARS-CoV-2 Mpro. This study aims to evaluate the inhibitory effects of Bofutrelvir on the E166N, E166R, His163A, E166V and S144A mutants of SARS-CoV-2 Mpro, as well as on MERS-CoV Mpro. Our findings indicate a substantial reduction in the inhibitory potency of Bofutrelvir against these mutants and MERS-CoV, with IC_{50} values significantly higher than those for the wild-type SARS-CoV-2 Mpro. Specifically, the E166N, E166R, E166V, S144A, and H163A mutations significantly reduce the binding affinity and inhibitory effectiveness of Bofutrelvir due to disrupted hydrogen bonds, altered binding site stability, and reduced enzyme activity. Structural analysis of the crystal complexes showed that changes in interactions at the S1 subsite in the mutants and the loss of hydrogen bonds at the S4 subsite in MERS-CoV Mpro are critical factors contributing to the diminished inhibitory activity. These insights reveal the necessity of ongoing structural analysis to adapt therapeutic strategies.

In 2002, the highly contagious severe acute respiratory syndrome (SARS) spread rapidly across the globe[1–3]. In 2012, another human coronavirus, the Middle East Respiratory Syndrome Coronavirus (MERS-CoV), emerged in the Middle East[4,5]. The COVID-19 pandemic, caused by the SARS-CoV-2 virus, began in 2019 and continues to have a significant global impact[6,7]. The COVID-19 pandemic has caused significant global disruption, leading to widespread illness, millions of deaths, and profound socioeconomic impacts[8,9]. The virus has overwhelmed healthcare systems and led to severe long-term health consequences for many survivors[10]. These circumstances highlight the importance of prevention, early detection, and appropriate treatment of COVID-19 or similar viruses like itself.

The target proteins of SARS-CoV-2 encompass both structural proteins, such as the spike (S), envelope (E), membrane (M), and nucleocapsid (N) proteins, and non-structural proteins, including RNA-dependent RNA polymerase (RdRp), papain-like protease (PLpro), main protease (Mpro), and helicase[11]. Among these, the main protease (Mpro), also referred to as the 3C-like protease (3CLpro), is critical for the viral replication cycle, rendering it a prime target for antiviral drug development[12]. Mpro is a cysteine protease that functions as a homodimer, with each monomer composed of three domains. Domains I and II feature antiparallel β-barrel structures that form a catalytic dyad constituted by Cys145 and His41[13,14]. This dyad is essential for the specific recognition and cleavage of the polyproteins at 11 distinct sites, generating the non-structural proteins nsp4 to nsp16, which are indispensable for viral genome replication and transcription[15]. The active site of Mpro, located in the cleft between domains I and II, includes four subsites (S1, S1', S2, S4). The crystal structure of SARS-CoV Mpro and its inhibitor complex was successfully elucidated[16]. Following the COVID-19 outbreak, the high-resolution structure of SARS-CoV-2 Mpro was determined[17]. Sequence alignment reveals a 96% homology between SARS-CoV and SARS-CoV-2 Mpro, underscoring a high degree of conservation[18]. This conservation makes Mpro an ideal target for the development of broad-spectrum antiviral agents against coronaviruses.

Based on the structure of SARS-CoV-2 Mpro inhibitors, they can be categorized into peptidomimetic, non-peptidomimetic, and natural product-based inhibitors[16]. Peptidomimetic inhibitors can further be divided into covalent and non-covalent inhibitors based on their interaction

[1]Shanghai Advanced Research Institute, Chinese Academy of Sciences, Shanghai, China. [2]Jiangxi Province Key Laboratory of Pharmacology of Traditional Chinese Medicine, School of Pharmacy, Gannan Medical University, Ganzhou, China. [3]Shenzhen Crystalo Biopharmaceutical Co, Ltd, Shenzhen, China. [4]Jiangxi Jmerry Biopharmaceutical Co, Ltd, Ganzhou, China. [5]These authors contributed equally: Weiwei Wang, Xuelan Zhou.[6]These authors jointly supervised this work: Qisheng Wang, Jian Li. ✉e-mail: wangqs@sari.ac.cn; rmsl_2040@163.com

modes[19]. Non-covalent peptidomimetic inhibitors typically bind through hydrogen bonds, van der Waals interactions, and hydrophobic interactions, offering high selectivity and low toxicity. Covalent peptidomimetic inhibitors bind to M[pro] through a two-step mechanism: first forming a non-covalent complex with the protease, followed by nucleophilic attack by Cys145 to form a covalent bond with the inhibitor's electrophilic warhead, such as Michael acceptors, aldehydes, nitriles, and α-ketoamides[20]. Bofutrelvir, also called FB2001, is a peptidomimetic inhibitor targeting the 3CL[pro] of the SARS-CoV-2, featuring an aldehyde warhead at the C-terminus. It can be administered via injection or inhalation, demonstrating broad-spectrum anti-coronavirus activity, a high resistance barrier, and higher drug concentrations in respiratory tissues and lungs compared to plasma[21]. Animal model studies have shown that Bofutrelvir significantly inhibits viral replication in the lungs and brain[22]. Given the remarkable attributes of Bofutrelvir, including its broad-spectrum anti-coronavirus activity, high resistance barrier, and superior concentration in respiratory tissues, it is essential to investigate its interactions with SARS-CoV-2 M[pro].

Mutations in SARS-CoV-2 M[pro] can significantly impact the efficacy of protease inhibitors, which are vital for antiviral treatment strategies[23,24]. To further understand the mechanisms of drug resistance and to aid in the development of more effective inhibitors, it is essential to study specific mutations within the M[pro] active site. The E166, S144, and H163 residues are located near the active site and have significant implications for inhibitor binding affinity and catalytic efficiency[25,26]. Recent studies have identified nirmatrelvir-resistant M[pro] mutants, highlighting S144 and E166 as key residues directly impacting nirmatrelvir inhibition[27–29]. Additionally, His163 mutations have been implicated in modulating enzymatic activity[23]. Among them, E166N and E166V exhibited the strongest resistance to nirmatrelvir, with IC$_{50}$ values of 3.429 μM (336.3-fold increase) and 1.908 μM (187.3-fold increase), respectively[30]. Resistance to nirmatrelvir was further confirmed for E166R in a yeast-based system[25]. Previous reports also documented S144A-mediated resistance to nirmatrelvir[27,28], while His163A substitutions have been associated with potential drug resistance mechanisms[31]. Consequently, investigating these mutations in SARS-CoV-2 M[pro] is pivotal for understanding drug resistance mechanisms and developing effective antiviral therapies. Here, we detemined the crystal structures of Bofutrelvir in complex with SARS-CoV-2 M[pro] mutants (E166N, E166R, H163A, E166V, and S144A) and MERS-CoV M[pro]. The E166N and E166R mutations are located near the active site of M[pro], and studying these mutations can help understand the roles of key residues in the catalytic process. These studies provide insights into the catalytic mechanism of M[pro], guiding drug design.

Similarly, the H163A mutation helps elucidate the specific function of position 163 histidine in enzyme activity. Investigating the inhibitory effects of Bofutrelvir on MERS-CoV and SARS-CoV-2 M[pro] mutants provides crucial information for the development of antiviral drugs. To further evaluate the inhibitory effects, FRET-based assays were used, showing significant reductions in Bofutrelvir's potency against these mutants compared to the wild-type M[pro]. Specifically, E166N and H163A mutations resulted in IC$_{50}$ values exceeding 100 μM, indicating a near-complete loss of efficacy, while E166R mutation had an IC$_{50}$ of 1.889 μM. Combined with a comprehensive analysis of the crystal structures of these complexes, the inhibitors showed a significant change in orientation in the binding pocket. The E166N mutation disrupted key hydrogen bonds, reducing stability and binding affinity. The E166R mutation altered the spatial configuration, and H163A eliminated critical hydrogen bonds, significantly weakening efficacy. Analysis of Bofutrelvir's interaction with MERS-CoV M[pro] showed an IC$_{50}$ of 12.11 μM, over 200-fold less effective than against SARS-CoV-2 M[pro]. Structural differences, particularly in the S4 subsite, contributed to reduced stability and efficacy. These results show the importance of specific residues in maintaining inhibitor binding and efficacy, providing insights for designing next-generation inhibitors to combat COVID-19 and related coronaviruses.

Results

Differential inhibitory effects of Bofutrelvir on various SARS-CoV-2 M[pro] mutants

Utilizing our previously established protocol[32], we successfully expressed and purified the M[pro]s from SARS-CoV-2 and MERS-CoV, as well as M[pro] mutants (including E166N, E166R, H163A, E166V and S144A) derived from SARS-CoV-2 (Fig. S1). The purification process yielded different M[pro] proteins at near homogeneity, as demonstrated by gel-filtration chromatography, with the results illustrated in Fig. S1. This comprehensive approach allowed us to obtain high-quality protein samples for further FRET and structural analyses.

To assess the inhibitory effects of Bofutrelvir on these mutated M[pro] variants, FRET-based assays were employed, providing a robust and sensitive measurement of protease activity. The experimental results demonstrated a notable reduction in the inhibitory potency of Bofutrelvir against the mutant M[pro] enzymes in comparison to the wild-type SARS-CoV-2 M[pro], for which we determined an IC$_{50}$ value of 0.021 μM[33]. Specifically, Bofutrelvir exhibited a dramatic loss of inhibitory capability against the E166N and H163A mutants, with IC$_{50}$ values exceeding 100 μM (Fig. 1a, c),
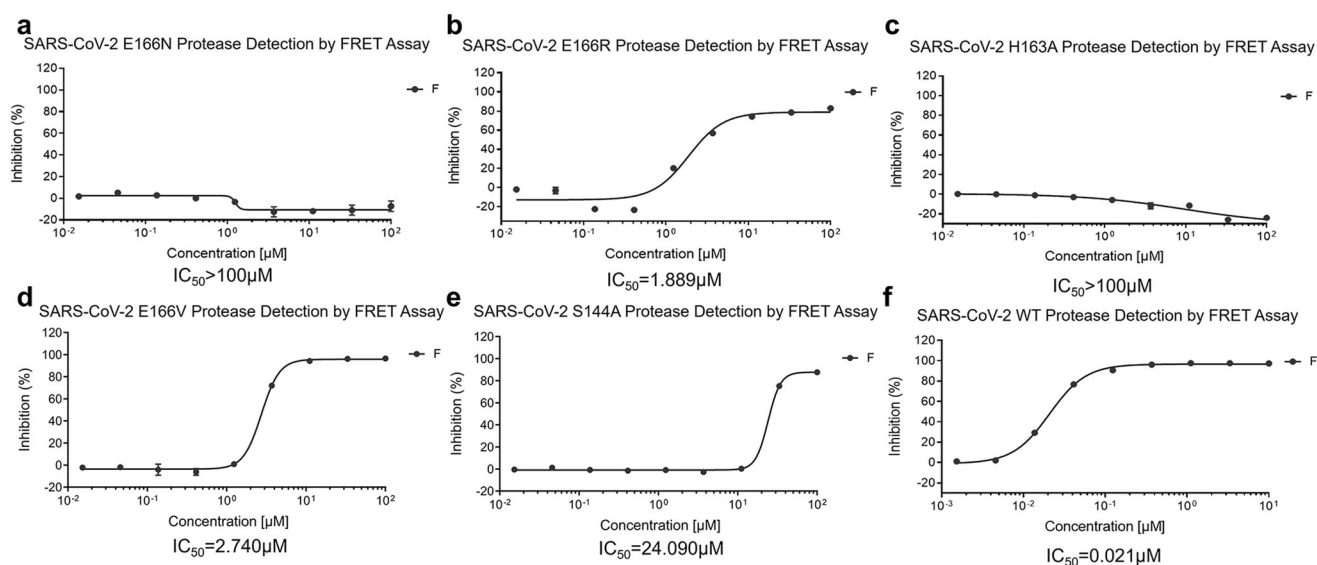

Fig. 1 | Differential inhibitory effects of Bofutrelvir on SARS-CoV-2 M[pro] variants. Inhibitory efficacy of Bofutrelvir on SARS-CoV-2 M[pro] E166N mutant (**a**), E166R Mutant (**b**), H163A mutant (**c**), E166V mutant (**d**), S144A mutant (**e**), and wild type (**f**).

Table 1 | Statistics for data processing and model refinement of SARS-CoV-2 Mᵖʳᵒ mutants or MERS-CoV Mᵖʳᵒ in complex with Bofutrelvir (cocrystal)

Name	SARS-CoV-2-E166N	SARS-CoV-2-E166R
PDB Code	8YWY	9INL
Beam line	BL10U2	BL10U2
Wavelength (Å)	0.97918	0.97918
Space group	C121	P1
a, b, c (Å)	113.42, 54.54, 45.50	55.32, 60.52, 63.15
α, β, γ (°)	90.00, 101.35, 90.00	89.49, 67.91, 70.40
Total reflections	111609	135824
Unique reflections	19797	44405
Resolution (Å)	1.95 (2.00–1.95)	2.04 (2.09–2.04)
R-merge (%)	9.6 (72.3)	11.5(61.9)
Mean I/σ (I)	13.5/2.5	5.7/1.9
Completeness (%)	99.0 (94.1)	97.6(96.0)
Redundancy	5.6(3.7)	3.1 (2.4)
Resolution (Å)	55.60–1.95	56.96–2.04
R_{work}/R_{free}(%)	19.99/24.64	20.89/25.58
Atoms	2417	4926
Mean temperature factor (Å²)	35.0	34.7
Bond lengths (Å)	0.007	0.007
Bond angles (°)	0.96	0.925
Ramachandran plot (%)		
Preferred	98.33	97.50
Allowed	1.67	2.50
outliers	0	0
Name	**SARS-CoV-2-H163A**	**SARS-CoV-2-E166V**
PDB Code	8YWZ	9LUG
Beam line	BL10U2	BL02U1
Wavelength (Å)	0.97918	0.97918
Space group	P212121	P212121
a, b, c (Å)	67.83, 102.80, 102.98	68.28, 101.73, 104.54
α, β, γ (°)	90.00, 90.00, 90.00	90.00, 90.00, 90.00
Total reflections	612026	533845
Unique reflections	56046	41514
Resolution (Å)	1.91 (1.96–1.91)	2.13 (2.19–2.13)
R-merge (%)	15.2 (105.2)	5.6 (164.2)
Mean I/σ (I)	16.6/2.50	9.5/2.5
Completeness (%)	99.1 (90.1)	100(100)
Redundancy	10.9 (6.5)	12.9 (13.2)
Resolution (Å)	30.63–1.91	72.91–2.13
R_{work}/R_{free}(%)	19.58/23.29	20.69/22.52
Atoms	4841	5028
Mean temperature factor (Å²)	36.1	30.75
Bond lengths (Å)	0.007	0.24
Bond angles (°)	0.98	3.19
Ramachandran plot (%)		
Preferred	98.30	98.49
Allowed	1.70	1.51
outliers	0	0
Name	**SARS-CoV-2-S144A**	**MERS-CoV**
PDB Code	9LUF	9INM
Beam line	BL02U1	BL10U2
Wavelength (Å)	0.97918	0.97918

Table 1 (continued) | Statistics for data processing and model refinement of SARS-CoV-2 Mᵖʳᵒ mutants or MERS-CoV Mᵖʳᵒ in complex with Bofutrelvir (cocrystal)

Name	SARS-CoV-2-S144A	MERS-CoV
Space group	P212121	P1211
a, b, c (Å)	68.08, 101.12, 104.31	93.19, 80.67, 100.55
α, β, γ (°)	90.00, 90.00, 90.00	90.00, 93.41, 90.00
Total reflections	619168	298525
Unique reflections	50168	61857
Resolution (Å)	1.99 (2.04–1.99)	2.34 (2.47–2.34)
R-merge (%)	4.2 (128.0)	17.0 (138.3)
Mean I/σ (I)	14.3/1.8	6.8/2.0
Completeness (%)	100 (99.9)	98.6 (97.9)
Redundancy	12.3 (9)	4.8(4.6)
Resolution (Å)	40.59–1.99	70.35–2.34
R_{work}/R_{free}(%)	19.98/23.07	22.79/27.48
Atoms	4974	9444
Mean temperature factor (Å²)	33.6	39.9
Bond lengths (Å)	0.23	0.010
Bond angles (°)	3.05	1.043
Ramachandran plot (%)		
Preferred	98.16	97.49
Allowed	1.84	2.51
outliers	0	0

Values in parentheses are for the highest-resolution shell.

indicating a near-complete abrogation of its inhibitory efficacy. In addition, the E166R, E166V, and S144A mutants retained some susceptibility to Bofutrelvir; however, the inhibitory potency was diminished, as evidenced by an increased IC$_{50}$ value of 1.889 μM, 2.740 μM and 24.090 μM, respectively (Fig. 1b, d, e).

Structural insights into the binding mechanisms of Bofutrelvir with SARS-CoV-2 Mᵖʳᵒ mutants

We are particularly interested in the effects of substituting glutamate at position 166 with arginine, valine or asparagine, which results in a nearly 90, 130, or over 4000-fold reduction in the inhibitory efficacy of Bofutrelvir against SARS-CoV-2. Similarly, substituting Serine at position 144 with Alanine or histidine at position 163 with alanine leads to an over 1000-fold or 4000-fold reduction in Bofutrelvir's inhibitory potency, despite E166, S144, and H163 not being directly involved in catalysis. To elucidate these effects, we determined the crystal structures of the Mᵖʳᵒ E166N-Bofutrelvir complex, the Mᵖʳᵒ E166R-Bofutrelvir complex, and the Mᵖʳᵒ H163A-Bofutrelvir complex, Mᵖʳᵒ E166V-Bofutrelvir complex, Mᵖʳᵒ S144A-Bofutrelvir complex, with resolutions of 1.95, 2.04, 1.91, 2.13 and 1.99 Å, respectively (Table 1). These complexes crystallized in the C121, P1, P212121, P212121 and P212121 space groups, respectively (Table 1). In the Mᵖʳᵒ E166N-Bofutrelvir complex structure, each asymmetric unit contains one Mᵖʳᵒ molecule, with the biological dimer generated through crystallographic symmetry. Conversely, each asymmetric unit in the Mᵖʳᵒ E166R-Bofutrelvir, Mᵖʳᵒ H163A-Bofutrelvir, Mᵖʳᵒ E166V-Bofutrelvir and Mᵖʳᵒ S144A-Bofutrelvir complex structures contains two Mᵖʳᵒ molecules. We extracted the monomeric structures from these fivemutant complexes with Bofutrelvir and performed structural superposition, revealing significant variations in the orientation of the inhibitor within the binding pocket (Fig. 2a). Magnifying the inhibitor binding pocket, it becomes apparent that the orientation of Bofutrelvir in the H163A mutant structure differs significantly from that in the other four mutants (Fig. 2b). Therefore, we displayed the inhibitor binding pocket in surface mode and highlighted the substrate-binding sites (S1', S1, S2, and S4) along with the mutation sites
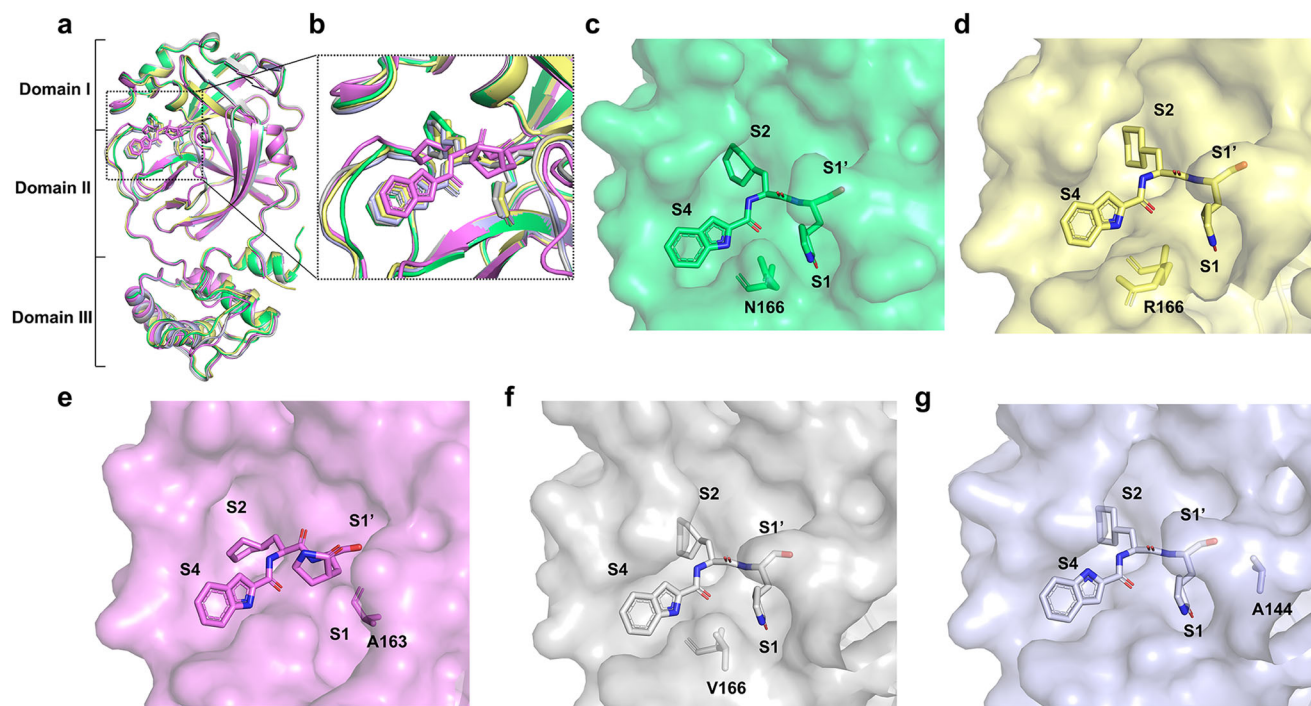
Fig. 2 | Crystal structure of SARS-CoV-2 Mᵖʳᵒ mutants in complex with Bofutrelvir. a Comparative analysis of the monomeric structures of SARS-CoV-2 Mᵖʳᵒ mutants bound to Bofutrelvir. Bofutrelvir is depicted in stick representation. The complexes are colored as follows: SARS-CoV-2 Mᵖʳᵒ E166N-Bofutrelvir in lime green, SARS-CoV-2 Mᵖʳᵒ E166R-Bofutrelvir in pale yellow, SARS-CoV-2 Mᵖʳᵒ H163A-Bofutrelvir in violet, SARS-CoV-2 Mᵖʳᵒ E166V-Bofutrelvir in gray and SARS-CoV-2 Mᵖʳᵒ S144A-Bofutrelvir inlightblue. The three domains of Mᵖʳᵒ are delineated with solid black lines, and the substrate-binding pocket is outlined with a black dotted box. **b** Enlarged view of the substrate-binding region. This panel highlights the detailed interactions within the substrate-binding pocket. **c** Surface representation of the substrate-binding subsites in SARS-CoV-2 Mᵖʳᵒ E166N mutant. The substrate-binding sites (S1', S1, S2, and S4) and the E166N mutation site are indicated. **d** Surface representation of the substrate-binding subsites in SARS-CoV-2 Mᵖʳᵒ E166R mutant. The substrate-binding sites (S1', S1, S2, and S4) and the E166R mutation site are shown. **e** Surface representation of the substrate-binding subsites in SARS-CoV-2 Mᵖʳᵒ H163A mutant. **f** surface representation of the substrate-binding subsites in SARS-CoV-2 Mᵖʳᵒ E166V mutant. **g** Surface representation of the substrate-binding subsites in SARS-CoV-2 Mᵖʳᵒ S144A mutant. The substrate-binding sites (S1', S1, S2, and S4) and the H163A mutation site are marked.

(Fig. 2c–g). Our analysis shows that the mutation sites E166, H163, and S144 are both located at S1, with E166N, E166R, E166V and S144A mutations exhibiting more consistent orientations that occupy the S1', S1, S2, and S4 pockets (Fig. 2c, d). In contrast, H163A shows substantial shifts in the S1', S1, and S2 pockets (Fig. 2e). Further comparison of these five mutant complex structures with the previously reported wild-type SARS-CoV-2 Mᵖʳᵒ-Bofutrelvir complex revealed that the orientation of Bofutrelvir in the H163A mutant structure is distinctly different from that in the wild-type and the other three mutants, particularly at the P1' site (aldehyde group), P1 site ((S)-γ-lactam ring), and P2 site (cyclohexyl moiety) (Fig. S2a, b, c). Additionally, the orientation of the E166R, E166V, and S144A mutants are closer to that of the wild-type in the P1'–P3 region compared to the E166N mutant (Figs. S2a, b, c and 2c, d).

Distinct interaction modes of Bofutrelvir in complex with wild-type and mutant SARS-CoV-2 Mᵖʳᵒ

To further elucidate the differential inhibitory capabilities of Bofutrelvir against three Mᵖʳᵒ mutants, we analyzed the binding interaction modes of Bofutrelvir with these mutants and the wild-type Mᵖʳᵒ (Fig. 3). Consistent with the wild-type, all mutants formed covalent bonds with Bofutrelvir. The electron density maps clearly indicated the positioning of Bofutrelvir within the ligand-binding cavity of both the wild-type and mutant Mᵖʳᵒ, where it is covalently linked to C145 via a C-S bond (Fig. S3a–e). At the S1' subsite, the interactions between Bofutrelvir and the E166N, E166R, S144A mutants, and the wild-type are similar, involving the formation of a thioether bond through the aldehyde group of Bofutrelvir interacting with the thiol group of C145 (Fig. 4a, b, e, f). The oxygen atom of the aldehyde group forms a crucial hydrogen bond with the C145 residue at the S1' site, stabilizing the inhibitor's conformation and providing essential support for intermolecular

binding. Additionally, the aldehyde oxygen atom forms hydrogen bonds with G143 and a water molecule. In the E166V mutant, the thiol group of C145 also forms a thioether bond with the aldehyde group of Bofutrelvir. The aldehyde oxygen establishes hydrogen bonds with both the C145 residue and a water molecule, but lacks the hydrogen bond interaction with G143 observed in the wild-type (Fig. 4d). However, the H163A mutant only forms the thioether bond with the aldehyde group of Bofutrelvir and the thiol group of C145, lacking the additional hydrogen bonds (Fig. 4c). At the S1 subsite, four mutants (E166N, E166R, H163A and E166V) lose the hydrogen bond between E166 and the NH group of the (S)-γ-lactam ring (Fig. 4a–f). However, the E166N, E166R, and E166V mutants retain a hydrogen bond between the NH group of the (S)-γ-lactam ring and Phe140, which is absent in the H163A and S144A mutant. The H172 of the E166V mutant can also form a hydrogen bond with the NH group of the (S)-γ-lactam ring through a water molecule. Furthermore, in the wild-type and the E166N, E166R, E166V, and S144A mutants, H163 forms a hydrogen bond with the carbonyl oxygen of the (S)-γ-lactam ring, with bond lengths less than 3 Å (Fig. 3a, b, d–f). In the H163A mutant, G143 forms a weaker hydrogen bond with the carbonyl oxygen of the (S)-γ-lactam ring, with a bond length greater than 3 Å (Fig. 3c). In the wild-type and the E166N, E166R, E166V and S144A mutants, the amino group between the S1 and S2 subsites forms a hydrogen bond with the carboxyl oxygen of His164, an interaction that is missing in the H163A mutant (Figs. 3 and 4). At the S2 subsite, the cyclohexyl moiety of Bofutrelvir stacks with the imidazole ring of His41. The cyclohexyl group is surrounded by the side chains of M49, Y54, M165, D187, and R188 in the wild-type and the E166N, E166R, E166V, and S144A mutants, creating extensive hydrophobic interactions. These hydrophobic interactions (M49 and Y54) are absent in the H163A mutant (Figs. 3 and 4)[22]. Additionally, the carbonyl oxygen between the S2 and
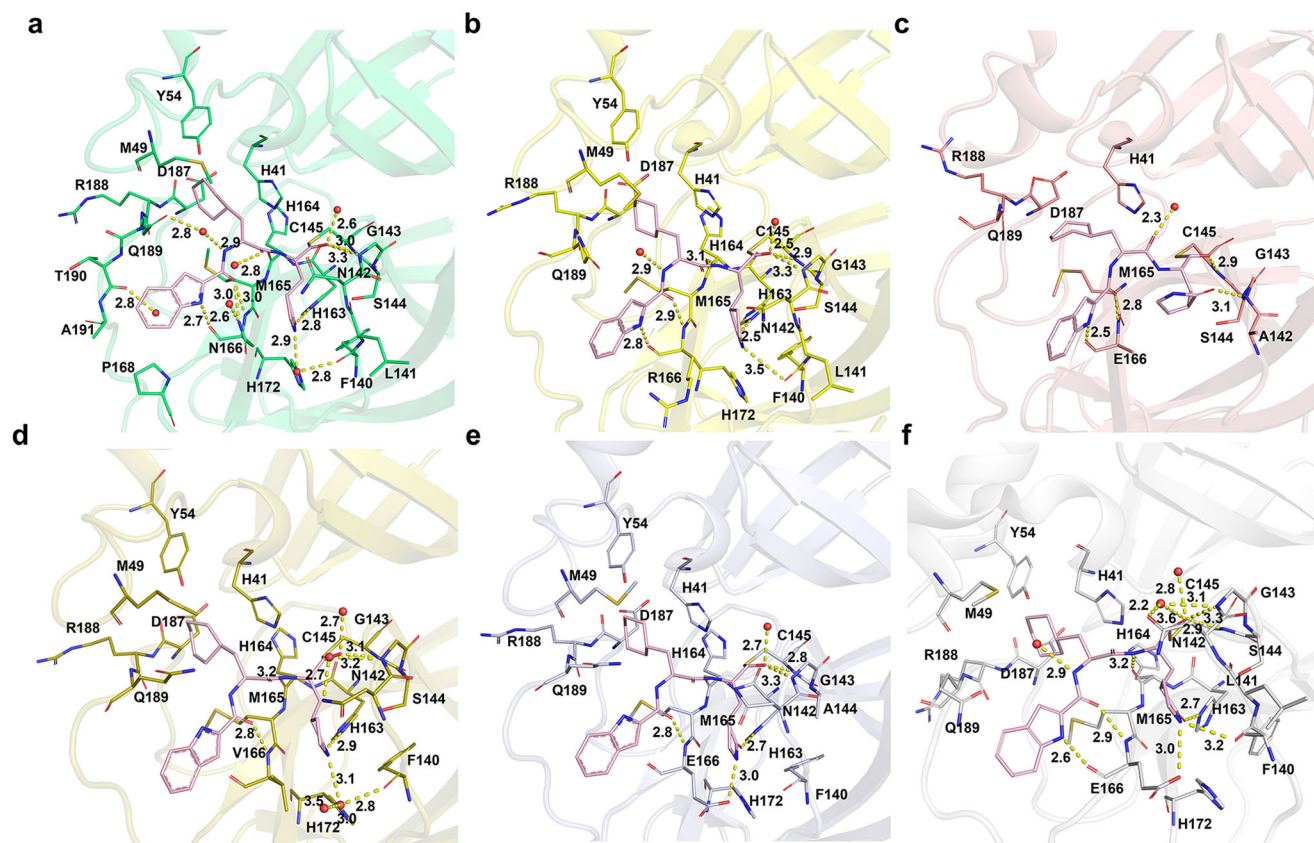
Fig. 3 | Detailed interactions of SARS-CoV-2 M^pro mutants in complex with Bofutrelvir. a SARS-CoV-2 M^pro E166N-Bofutrelvir complex. Binding residues (within 4 Å) are shown as lime green sticks. Bofutrelvir is in light pink. Water molecules are in red licorice, with hydrogen bonds as yellow dashed lines. **b** SARS-CoV-2 M^pro E166R-Bofutrelvir complex. Binding residues are pale yellow sticks. Bofutrelvir is in light pink. Water molecules are in red licorice, with hydrogen bonds as yellow dashed lines. **c** SARS-CoV-2 M^pro H163A-Bofutrelvir complex. Binding residues are violet sticks. Bofutrelvir is in light pink. Water molecules are in red licorice, with hydrogen bonds as yellow dashed lines. **d** SARS-CoV-2 M^pro E166V-Bofutrelvir complex. Binding residues are olive sticks. Bofutrelvir is in light pink. Water molecules are in red licorice, with hydrogen bonds as yellow dashed lines. **e** SARS-CoV-2 M^pro S144A-Bofutrelvir complex. Binding residues are lightblue sticks. Bofutrelvir is in light pink. Water molecules are in red licorice, with hydrogen bonds as yellow dashed lines. **f** SARS-CoV-2 M^pro-Bofutrelvir complex (PDB: 6LZE). Binding residues are gray sticks. Bofutrelvir is in light pink. Water molecules are in red licorice, with hydrogen bonds as yellow dashed lines.

S4 subsites forms hydrogen bonds with the amino group of Glu166, Asn166, or Arg166 in both the wild-type and mutant forms. At the S4 subsite, the indole moiety of Bofutrelvir forms hydrogen bonds with Glu166, Asn166, or Arg166 in both the wild-type and mutants E166N, E166R, His163A. However, in the E166V and S144A mutants, the indole moiety of Bofutrelvir does not participate in the formation of hydrogen bonds. In general, the binding models of Bofutrelvir with the E166N, E166R, and H163A mutants reveal that Bofutrelvir adopts a relatively stable conformation at the S4 subsite, while exhibiting more flexible conformations at the S1', S1, and S2 subsites. Among the mutants, the H163A mutation induces the most significant conformational changes.

Analysis of the Impact of E166/H163/S144 Mutations on the Stability of the S1 Subsite and Inhibitor Binding Mode

Given the role of E166 in stabilizing the S1 subsite, we further investigated how mutations E166R, E166N, and E166V affect the stability of the S1 pocket or alter the binding mode of inhibitors. In the unmutated M^pro, E166 is a critical residue that stabilizes the S1 subsite through interactions with the N-terminal serine residue of the adjacent protomer. In the structure of the wild-type M^pro-Bofutrelvir, the E166 plays an important role as a key structural unit that fills the S1 subsite and participates in the binding of Bofutrelvir or substrates[22]. In this structure, the side chain of E166 forms five hydrogen bonds (Fig. 5a), including one hydrogen bond with the NH of the (S)-γ-lactam ring of Bofutrelvir, one with the carbonyl oxygen between the S2 and S4 subsites, and one involving the indole moiety of Bofutrelvir in its

binding, all three of which are involved in binding to Bofutrelvir. The other two hydrogen bonds maintain the correct conformation of the S1 subsite by connecting E166 with the N-terminal serine residue of the adjacent protomer and the NH group of the imidazole ring of H172. This interaction is crucial for maintaining the correct conformation of the S1 pocket. However, when E166 is replaced by N166/R166/V166, we observe that the five hydrogen bonds mentioned above are disrupted and/or altered (Fig. 5b–d). In the complex structures of E166N/E166R/E166V mutants with Bofutrelvir, the hydrogen bonds connecting N166/R166/V166 with the N-terminal serine residue of the adjacent protomer and the NH group of the imidazole ring of H172 disappear, with the disappearance of the N-terminal serine residue of the adjacent protomer due to the lack of electron density. Importantly, with the mutation of E166, the hydrogen bond connecting E166 and the NH of the (S)-γ-lactam ring of Bofutrelvir is also destroyed. All these changes lead to decreased stability of the S1 pocket, drastically reduced binding of Bofutrelvir, and thus strong resistance to Bofutrelvir (Fig. 5b–d).

Furthermore, we investigated how His163 and S144 affect the stability of the S1 pocket or alter the binding mode of inhibitors. In the unmutated M^pro, H163 also plays a critical role in binding Bofutrelvir, forming a hydrogen bond with the carbonyl oxygen of the (S)-γ-lactam ring of Bofutrelvir and participating in π–π stacking between F140 and H163. Additionally, H163 forms hydrogen bonds with G146, S147, and Y161 to stabilize the S1 subsite (Fig. 5e). However, when H163 is mutated to A163, the hydrogen bond between H163 and Bofutrelvir is completely destroyed, the π–π stacking between F140 and H163 is also completely disrupted, and
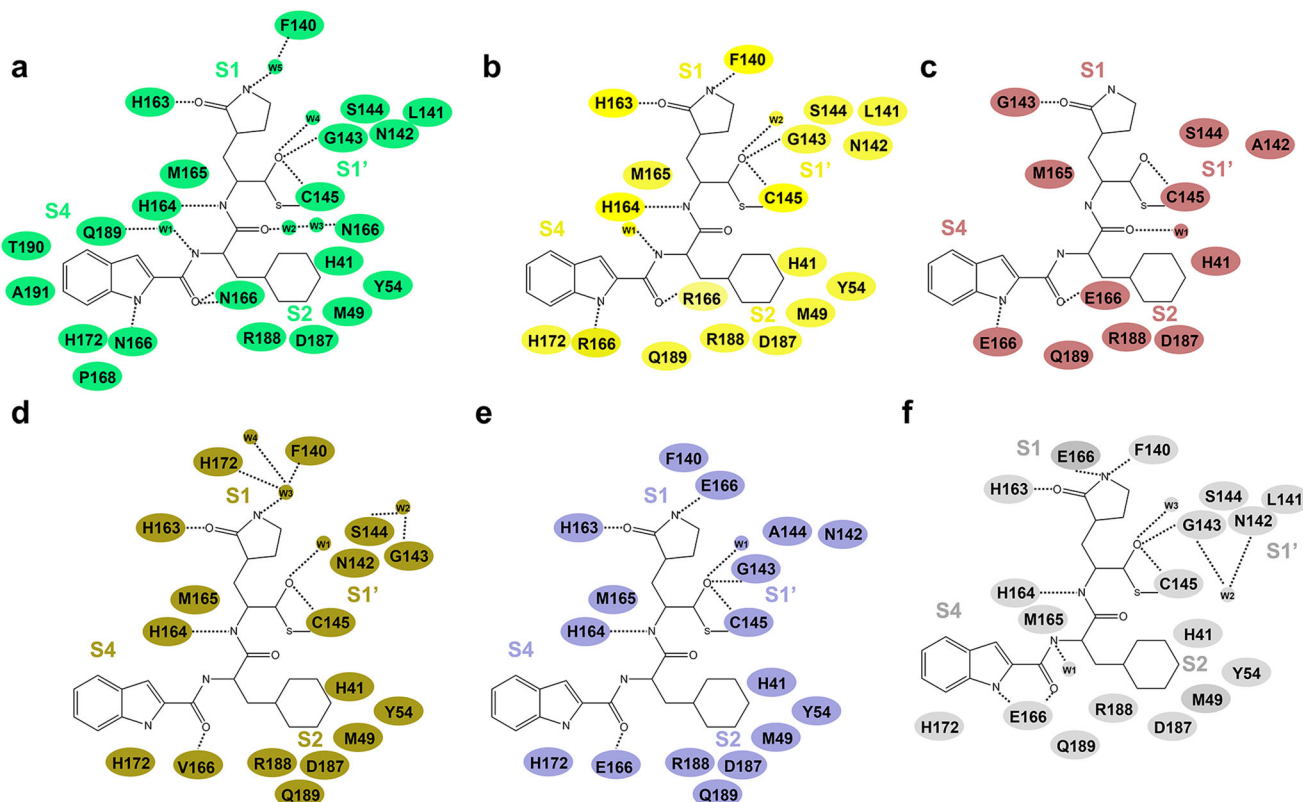
Fig. 4 | The schematic interaction between Bofutrelvir and SARS-CoV-2 M^pro mutants. a A schematic interaction between Bofutrelvir and SARS-CoV-2 M^pro E166N. **b** Interaction with E166R mutant. A precise illustration of the interaction between Bofutrelvir and the SARS-CoV-2 M^pro E166R variant. **c** Schematic representation of the interaction between Bofutrelvir and the SARS-CoV-2 M^pro H163A variant. **d** Schematic representation of the interaction between Bofutrelvir and the SARS-CoV-2 M^pro E166V variant. **e** Schematic representation of the interaction between Bofutrelvir and the SARS-CoV-2 M^pro S144A variant. **f** A schematic interaction between Bofutrelvir and SARS-CoV-2 M^pro (PDB:6LZE). Water molecules are depicted as solid circles.
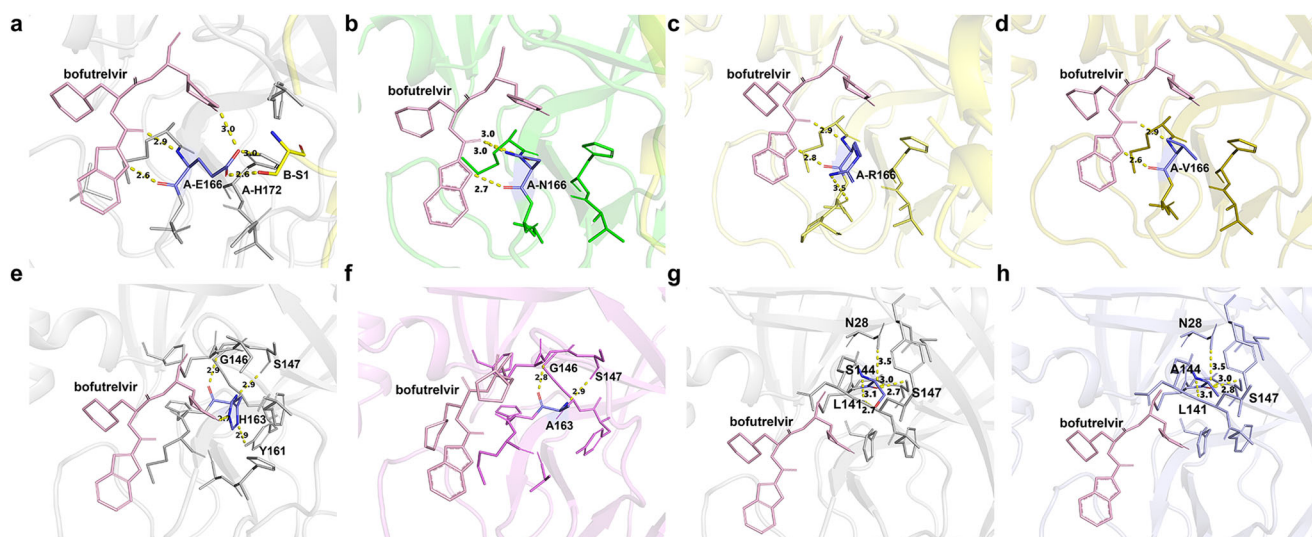

Fig. 5 | Comparison of the structures of the WT M^pro-Bofutrelvir and mutants-Bofutrelvir complexes in S1 pocket. a The structure of the S1 pocket of the WT-E166-M^pro-Bofutrelvir complex (PDB:6LZE). **b** The structure of the S1 pocket of the E166N-M^pro-Bofutrelvir complex. **c** The structure of the S1 pocket of the E166R-M^pro-Bofutrelvir complex. **d** The structure of the S1 pocket of the E166V-M^pro-Bofutrelvir complex. **e** The structure of the S1 pocket of the WT-H163-M^pro-Bofutrelvir complex (PDB:6LZE). **f** The structure of the S1 pocket of the H163A-M^pro-Bofutrelvir complex. **g** The structure of the S1 pocket of the WT-S144-M^pro-Bofutrelvir complex (PDB:6LZE). **h** The structure of the S1 pocket of the S144A-M^pro-Bofutrelvir complex.

the hydrogen bond formed between H163 and Y161 is destroyed (Fig. 5f). These changes lead to a significant decrease in the stability of the S1 pocket and drastically reduced binding of Bofutrelvir, resulting in even stronger resistance to Bofutrelvir. For the S144A mutant, when the hydroxyl group of

the serine residue is replaced by alanine, the hydrogen bond between this hydroxyl group of S144 and the main chain carbonyl of L141 is eliminated (Fig. 5g, h). This change affects the stability of the S1 subsite, reducing the binding affinity for Bofutrelvir and leading to drug resistance.
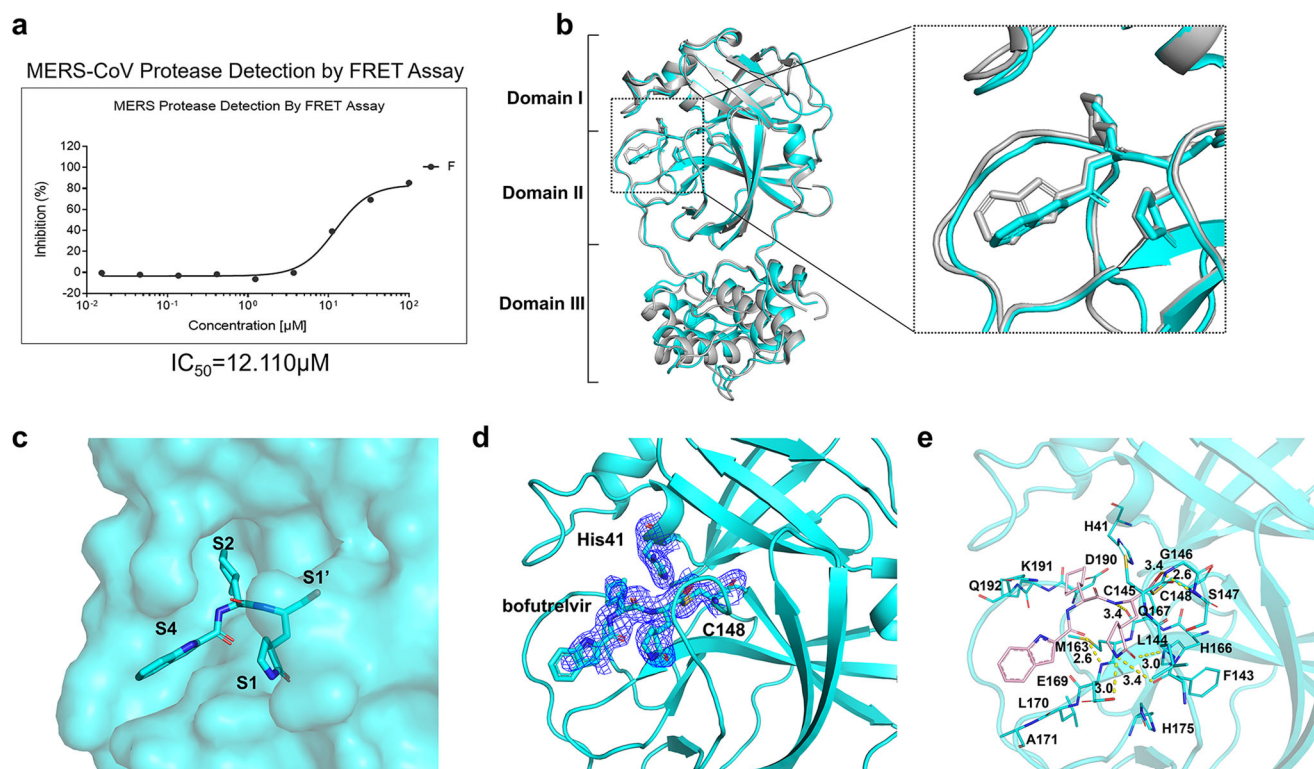
Fig. 6 | Inhibitory mechanism of Bofutrelvir against MERS-CoV M^pro.
a Inhibitory effects of Bofutrelvir on MERS-CoV M^pro. A representation of the inhibitory activity of Bofutrelvir against the MERS-CoV main protease. **b** Structural alignment of M^pro complexes with Bofutrelvir from MERS-CoV and SARS-CoV-2. The MERS-CoV M^pro-Bofutrelvir complex is shown in cyan, while the SARS-CoV-2 M^pro-Bofutrelvir complex is shown in gray. A detailed view of the substrate-binding pocket is provided. **c** Surface representation of the substrate-binding subsites in MERS-CoV M^pro. The subsites S1', S1, S2, and S4 are indicated. **d** The 2Fo-Fc Density Map of Bofutrelvir with Catalytic Dyad (H41 and C148). Illustrated as a blue mesh, outlined at a contour level of 1.0 σ. **e** Detailed interactions of the MERS-CoV M^pro-Bofutrelvir Complex. Residues involved in inhibitor binding (within 4 Å) are presented in stick form. Bofutrelvir is in light pink. Hydrogen bond interactions are depicted as yellow dashed lines.

Structural analysis of Bofutrelvir interaction with MERS-CoV M^pro

To measure the inhibitory effects of Bofutrelvir on MERS-CoV M^pro, we employed FRET-based assays, which provide a robust and sensitive evaluation of protease activity. The results demonstrated a substantial reduction in the inhibitory potency of Bofutrelvir against MERS-CoV M^pro. Specifically, Bofutrelvir showed a dramatic loss of inhibitory capability, with an IC$_{50}$ value of 12.11 μM (Fig. 6a), indicating a more than 200-fold decrease in efficacy compared to its activity against SARS-CoV-2 M^pro. This significant reduction in inhibitory potency suggests that structural differences between MERS-CoV M^pro and SARS-CoV-2 M^pro critically impact the binding efficiency of Bofutrelvir. Consequently, we determined the crystal structure of MERS-CoV M^pro in complex with Bofutrelvir. The structure of MERS-CoV M^pro with Bofutrelvir, belonging to space groups P1211, were resolved to a resolution of both 2.34 Å, as detailed in Table 1. In its structure, each asymmetric unit contains four M^pro molecules. By extracting the monomeric MERS-CoV M^pro molecules and comparing them with SARS-CoV-2 M^pro, we found differences in the orientation of Bofutrelvir and in domain III (Fig. 6b). Enlarging the inhibitor binding pocket revealed that the orientation of Bofutrelvir in the MERS-CoV structure differs significantly from that in SARS-CoV-2, especially in the orientation of the indole moiety (Fig. 6b). Further, we displayed the inhibitor binding pocket in surface mode and highlighted the substrate-binding sites (S1', S1, S2, and S4) and the mutation site (Fig. 6c). We found that the orientation of Bofutrelvir in the S4 pocket shows a marked shift compared to that in SARS-CoV-2 (Fig. 6c and Fig S2c).

To further elucidate the inhibitory mechanism of Bofutrelvir against MERS-CoV M^pro, we conducted a detailed analysis of the binding interaction modes of Bofutrelvir with MERS-CoV M^pro (Figs. 6e and 7a). Similar to SARS-CoV-2 M^pro, MERS-CoV M^pro forms a covalent bond with Bofutrelvir. The electron density maps clearly show Bofutrelvir positioned in the ligand-binding cavities of both MERS-CoV M^pro and SARS-CoV-2 M^pro, covalently linked to C145 through a C-S bond (Fig. 6d). At the S1' subsite, the interactions between MERS-CoV M^pro and Bofutrelvir resemble those seen with SARS-CoV-2 M^pro, where the aldehyde group of Bofutrelvir interacts with the thiol group of C145, forming a thioether bond (Fig. 7a, b). The oxygen atom of the aldehyde forms a hydrogen bond with the Cys145 residue at the S1' site, which is crucial for maintaining conformational stability of the inhibitor and providing essential support for intermolecular binding. Additionally, the aldehyde oxygen atom forms a hydrogen bond with G146. However, MERS-CoV M^pro lacks the interaction with water molecules at the S1 site, resulting in the absence of three hydrogen bonds (Figs. 7a, b). At the S1 subsite, the interactions between MERS-CoV M^pro and Bofutrelvir are largely consistent with those observed in SARS-CoV-2 M^pro, including hydrogen bonds between E169 and the NH group of the (S)-γ-lactam ring, Phe143 and the NH group of the (S)-γ-lactam ring, and H166 with the carbonyl oxygen of the (S)-γ-lactam ring. At the S2 site, the cyclohexyl moiety of Bofutrelvir stacks with the imidazole ring of His41 and is surrounded by the side chains of M49, Y54, M168, D190, H175, and K191, generating extensive hydrophobic interactions (Fig. 7a, b). However, MERS-CoV M^pro lacks the hydrophobic interactions with residues homologous to M49 and Y54 found in SARS-CoV-2 M^pro. Lastly, at the S4 subsite, MERS-CoV M^pro lacks the hydrogen bond between E169 and the indole moiety of Bofutrelvir, leading to no hydrogen bond formation at the S4 site and consequently, a more than 200-fold decrease in inhibitory activity. Overall, the binding model of Bofutrelvir with MERS-CoV M^pro reveals that the conformation of Bofutrelvir at the S4 subsite is the least stable, with the absence of hydrogen bonds leading to conformational changes and weakened inhibitory capability.

Fig. 7 | Schematic Interaction of Bofutrelvir with MERS Mᴾʳᵒ. a The interaction between Bofutrelvir and the MERS Mᴾʳᵒ, depicted schematically. **b** A detailed schematic showing the interaction between Bofutrelvir and SARS-CoV-2 Mᴾʳᵒ. Water molecules are depicted as solid circles.
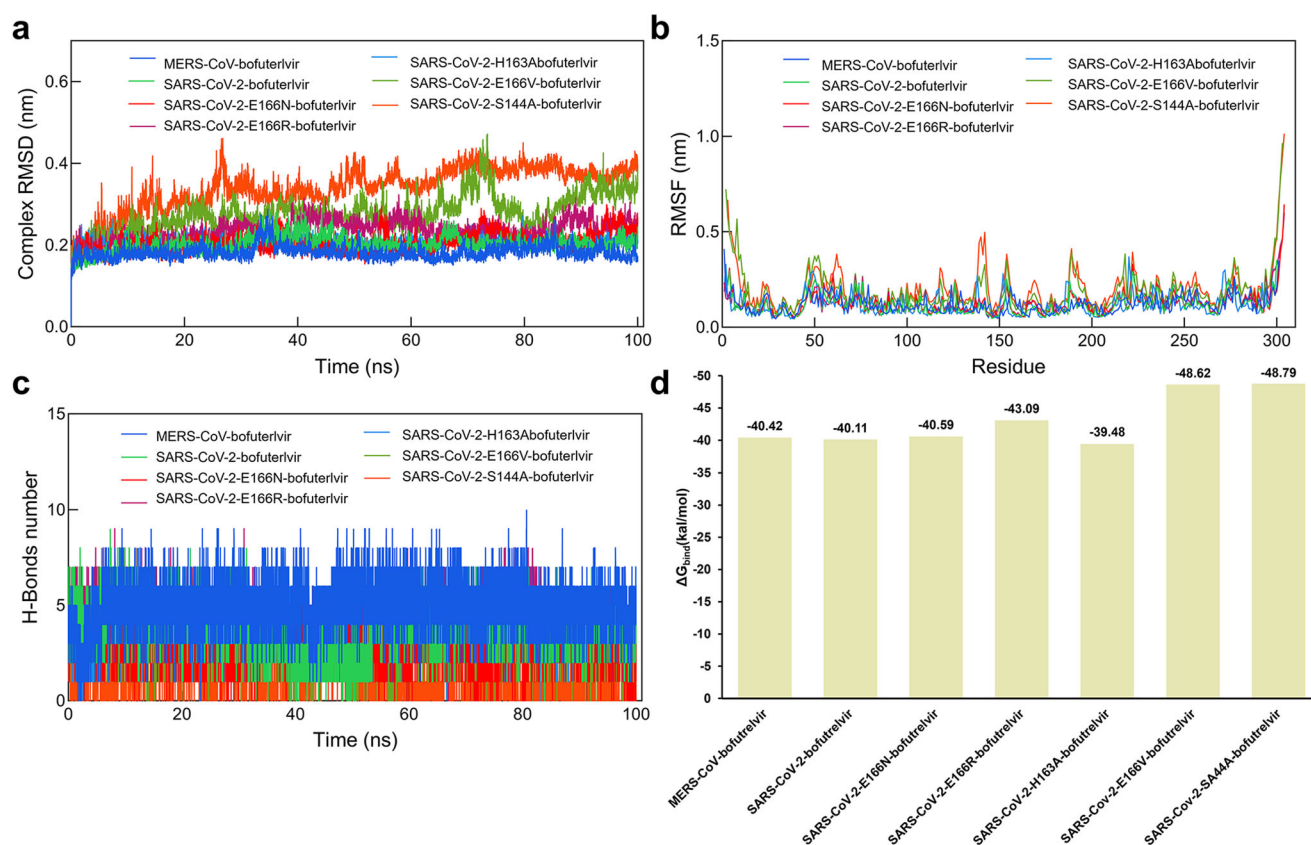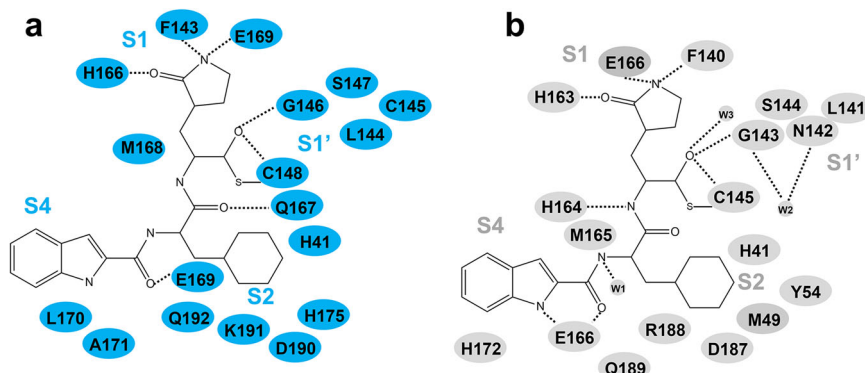

Fig. 8 | Analysis of the molecular dynamics simulation (100 ns) of Bofutrelvir in complex with various Mᴾʳᵒ. a RMSD curve of Bofutrelvir in complex with various Mᴾʳᵒ, **b** RMSF curve of various Mᴾʳᵒ, **c** Hydrogen bond variation curve of the various complex (Bofutrelvir in complex with various Mᴾʳᵒ). **d** The average binding free energy (kcal/mol) of seven complexes calculated using the MM/PBSA method.

The binding affinity and free energy of Bofutrelvir to different Mᴾʳᵒ

Although crystallographic evidence confirms the binding capability of Bofutrelvir to the Mᴾʳᵒ of SARS-CoV-2 (including its mutants) and MERS-CoV, substantial variations in inhibitory efficacy were observed among these targets. To elucidate the mechanistic basis of these differential binding affinities, MD simulations were performed over a 100 ns trajectory, followed by rigorous binding free energy calculations using the MM-PBSA/GBSA framework. From the RMSD (root mean square deviation) curves, the complexes of Mᴾʳᵒ from SARS-CoV-2 and its mutants, as well as Mᴾʳᵒ from MERS-CoV with Bofutrelvir, all exhibit relatively stable structures, with an RMSD difference not exceeding 0.3 nm (Fig. 8a). Root-mean-square fluctuation (RMSF) measurements further characterized residue-specific flexibility patterns. While localized regions of elevated flexibility were detected in both MERS-CoV and SARS-CoV-2 Mᴾʳᵒ mutants, the majority of catalytic domains demonstrated constrained fluctuations, particularly in conserved substrate-binding subsites (Fig. 8b). The number of hydrogen bonds is used to determine the stability of protein-ligand complexes. During the 100 ns molecular simulation, MERS-CoV, SARS-CoV-2, and their mutants formed a relatively stable number of hydrogen bonds with the Bofutrelvir, indicating strong binding between them (Fig. 8c).

Furthermore, the binding free energies of the complexes were calculated and analyzed using the MM/PBSA method. The results demonstrated that both MERS-CoV and SARS-CoV-2 Mᴾʳᵒ and their mutants exhibited strong binding stability with Bofutrelvir, as evidenced by the negative values of the total binding free energies (Fig. 8d). Specifically, the binding free energies were −40.42 kcal/mol for the MERS-CoV-2-E166V-bofutrelvir complex, −40.11 kcal/mol for the SARS-CoV-2-bofutrelvir complex, −40.59 kcal/mol for the SARS-CoV-2-E166N-bofutrelvir complex, −43.09 kcal/mol for the SARS-CoV-2-E166R-bofutrelvir complex, −48.62 kcal/mol for the SARS-CoV-2-E166V-bofutrelvir complex,

−48.76 kcal/mol for the SARS-CoV-2-S144A-bofutrelvir complex, and −39.48 kcal/mol for the SARS-CoV-2-H163A-bofutrelvir complex.

Discussion

The impact of SARS-CoV-2 on humanity is well-documented[34,35]. Despite the currently low mortality rate of SARS-CoV-2, various coronaviruses continue to pose significant threats to human and animal health. Notable outbreaks such as SARS-CoV in 2002, MERS-CoV in 2012, and the ongoing SARS-CoV-2 pandemic have resulted in substantial global disruption[1,4,7]. Consequently, it remains imperative to maintain vigilance and develop more effective coronavirus inhibitors. The M[pro] of SARS-CoV-2 plays a crucial role in viral replication by cleaving viral polyproteins[36]. M[pro] is highly conserved among known coronaviruses and lacks structural homology with the human proteome, making it an ideal target for therapeutic research[37]. Accordingly, the number of inhibitors targeting M[pro] is steadily increasing. In this context, as the use of M[pro] inhibitors increases, there is growing concern about drug-resistant mutations[23,25,38]. The selection pressure for these resistant mutations will continue to rise and may exceed the currently known set of resistance variants[23,38]. Therefore, understanding how these mutants affect drug resistance is crucial for optimizing drug design. The E166 residue is considered a potential hotspot for drug resistance[39,40]. Although E166 does not directly participate in catalysis, it has a significant impact on enzyme function and drug sensitivity[30,39]. It is indicated that different mutations at the E166 site produce varying effects on drug resistance[25,41]. For example, the E166N, E166R and E166V mutations significantly enhance resistance to nirmatrelvir, highlighting the substantial impact of E166 on drug sensitivity[25,27,28,30,40]. Meanwhile, the H163 residue plays a critical role in inhibitor binding[26,31,42]. The H163A mutant shows a significant reduction in affinity for multiple inhibitors, underscoring the importance of H163 in inhibitor binding[26,43,44]. In addition to mutations related to Glu166, S144A also confers resistance to nirmatrelvir[27]. Therefore, studying the E166, S144 and H163 mutant not only provides valuable information for addressing resistance mutations but also advances the development and optimization of innovative drugs.

Bofutrelvir is a peptidomimetic inhibitor targeting the M[pro] of SARS-CoV-2 and is considered to have broad-spectrum antiviral activity against coronaviruses[21,45]. Investigating its interaction with various coronavirus M[pro] and M[pro] mutants is essential for understanding its mechanism of action and optimizing its therapeutic potential against SARS-CoV-2 and other related viruses. In our study, we assessed the inhibitory effects of Bofutrelvir on SARS-CoV-2 M[pro] mutants (E166N, E166R, H163, E166V and S144A) and MERS-CoV M[pro]. The results demonstrated a significant reduction in the inhibitory potency of Bofutrelvir against SARS-CoV-2 M[pro] mutants (E166N, E166R, H163, E166V, and S144A) and MERS-CoV M[pro] (Figs. 1 and 6a). Specifically, at the S1 subsite, four mutants (E166N, E166R, E166V, and H163A) lacked the hydrogen bond between E166 and the NH group of the (S)-γ-lactam ring, and S144A or His163 loses a hydrogen bond between the NH group of the (S)-γ-lactam ring and Phe140, resulting in a marked decrease in inhibitory activity (Fig. 4). At the S4 subsite, MERS-CoV M[pro] lacked the hydrogen bond between E169 and the indole group, leading to a more than 200-fold reduction in inhibitory potency (Fig. 7). Overall, in the models of Bofutrelvir binding to E166N, E166R, E166V, S144A and H163A mutants, Bofutrelvir exhibited a relatively stable conformation at the S4 subsite but was more flexible at the S1', S1, and S2 subsites, especially the S1 subsites, with the H163A mutation causing the most significant conformational changes (Figs. 2, 3, 4) In the model of Bofutrelvir binding to MERS-CoV M[pro], the conformation at the S4 subsite was the least stable, with the absence of hydrogen bonds resulting in conformational changes and reduced inhibitory capacity (Fig. 6). The E166N and H163A mutants were completely resistant to Bofutrelvir. However, Bofutrelvir could still form stable complexes with these mutants because the E166N and H163A mutations did not significantly alter the overall conformation of the protein, allowing it to still bind to Bofutrelvir (Fig. 2a), which has also been demonstrated by molecular dynamics simulations (Fig. 8). Furthermore,

although the key interactions of Bofutrelvir at the S1 site were significantly weakened in the E166N and H163A mutants compared to the wild type (Fig. 4), the remaining interactions (especially the covalent bonds formed with C145) were still able to maintain the stability of the complex under crystallization conditions. This indicates that even if the Bofutrelvir binds stably to the active site of E166N and H163A mutants, its inhibitory effectiveness can still be reduced if the interactions are not sufficiently strong or effective. Notably, in our structure, the N-Finger was not observed in any of them, except for MERS-CoV. The lack of electron density for the N-terminal residues (Ser1/Gly2) under non-physiological pH might destabilize the N-finger, potentially exacerbated by an uncleaved His-tag increasing flexibility, as seen in structures like 7CBT, 7DQZ, and 7VLQ where N-terminal density is missing[46–49].

The E166N mutation, which replaces glutamic acid (E) with asparagine (N), disrupts not only the hydrogen bond connecting E166 to the (S)-γ-lactone ring NH of Bofutrelvir but also two crucial hydrogen bonds formed with the N-terminal serine residue of an adjacent protomer and the NH group of the H172 imidazole ring. This disruption leads to a significant decrease in the stability of the S1 subsite and a sharp reduction in Bofutrelvir's binding affinity, resulting in strong resistance to Bofutrelvir (as shown in Figs. 1a, 3a, 4a, and 5b). Furthermore, compared to the wild-type M[pro], the catalytic efficiency (measured by the kinetic parameter k_{cat}/K_m) of the E166N mutant is reduced by ~84-fold, while the reductions for the E166R or E166V mutants are relatively smaller, at about 16-fold or 10-fold, respectively[25]. This suggests that the E166N mutation causes a greater reduction in enzymatic activity compared to E166R and E166V, which better explains why the IC$_{50}$ value of E166N for Bofutrelvir is higher and its inhibitory capacity is greatly reduced. Additional study has reported that the enzymatic activity of the E166V mutant is significantly decreased when cleaving the substrate, with a k_{cat}/K_m value of only 3% of that of the wild-type M[pro][27]. Based on the hypothesis that the E166N mutation causes an even greater reduction in enzymatic activity, it is plausible that the k_{cat}/K_m value of E166N is lower than that of the wild-type M[pro], which may contribute to a significant increase in the IC$_{50}$ value of E166N for Bofutrelvir. Our experimental results indicate that the E166N mutation significantly decreases the binding affinity of the inhibitor, thereby greatly diminishing its inhibitory effect. Specifically, the IC$_{50}$ value of Bofutrelvir for the E166N mutant exceeds 100 μM, whereas the IC$_{50}$ value for the wild type is only 0.021 μM, indicating a substantial drop in efficacy (see Fig. 1a, f). This finding underscores the crucial role of E166 in inhibitor binding, despite its indirect involvement in the catalytic process. Similarly, the E166R mutation, which replaces glutamic acid with arginine (R), introduces a larger and positively charged side chain. This alteration significantly interferes with Bofutrelvir binding by modifying the spatial configuration of the binding site. Our results demonstrate that the E166R mutation conferred resistance to Bofutrelvir, with the IC$_{50}$ value increasing 89-fold compared to the wild-type M[pro] (Figs. 1b, f and 3b). This mutation not only disrupts existing interactions but also may form salt bridges or electrostatic interactions, potentially explaining why Bofutrelvir retains some inhibitory capacity against E166R. In terms of enzyme activity of the E166R mutant, the catalytic efficiency (k_{cat}/K_m) is reduced by ~16-fold compared to the wild-type M[pro][25]. In the E166V mutation, the substitution of glutamic acid with hydrophobic valine leads to alterations in the original five hydrogen bonds (Figs. 3d, 4d and 5e). This structural change significantly disrupts the binding of Bofutrelvir by adjusting the spatial conformation of the binding site. Compared to asparagine, the -CH$_3$ side chain of valine may enhance hydrophobic interactions. Meanwhile, the hydrophobic interaction formed by V166 may be weaker than the electrostatic interaction of R166, which could be one reason why the IC$_{50}$ value of E166V is higher than that of E166R but lower than that of E166N. Our research results indicate that the E166V mutation results in high resistance to Bofutrelvir, with an IC$_{50}$ value increased by 130 times compared to the wild-type M[pro] (Figs. 1d, f). Additionally, the enzymatic activity parameter (k_{cat}/K_m) of E166V varies widely, ranging from a 10-fold to over 90-fold decrease[25,27]. Overall, although the E166N, E166R, and E166V mutants all exhibit some degree of resistance to

Bofutrelvir, the E166N mutation has a more pronounced impact on enzymatic activity.

Nirmatrelvir specifically inhibits the M^pro of SARS-CoV-2 and is approved as an effective treatment for COVID-19[50,51]. Recent studies have reported that the E166V and S144A substitutions in M^pro confer resistance to nirmatrelvir, with E166V conferring the strongest resistance but also impairing viral replicative fitness. Our study also demonstrates that E166V and S144A confer resistance to Bofutrelvir, sharing some similarities and differences in resistance profiles. Structurally, Bofutrelvir possesses an aldehyde group as a warhead, suggesting that covalent interactions should be stronger than those contributed by a nitrile group in Nirmatrelvir (Fig. S4a, b). Similarly, in terms of inhibitory capacity, the IC_{50} of Bofutrelvir and nirmatrelvir against wild-type virus are 0.021 μM and 0.051 μM[28,33], respectively, indicating that the IC_{50} of nirmatrelvir is 2.4 times that of Bofutrelvir. From the surface representations of wild-type SARS-CoV-2 M^pro in complex with Bofutrelvir and Nirmatrelvir, it is evident that the additional P3 of Nirmatrelvir does not directly participate in binding with M^pro (Fig. S4c)[22,52]. For the E166V mutant, resistance to both Bofutrelvir and nirmatrelvir is conferred, leading to a significant increase in the IC_{50} values of Bofutrelvir and nirmatrelvir by 130-fold and 218-fold, respectively[27]. Structural analysis reveals that the substitution of E166 with valine disrupts key hydrogen bonds between Bofutrelvir and nirmatrelvir, causing E166V to deviate markedly from the S1 site compared to the wild-type (Fig. S4d), resulting in a sharp decline in inhibitory capacity and the development of strong resistance. For the S144A mutant, resistance to both Bofutrelvir and nirmatrelvir is also conferred. However, the resistance of the S144A mutant to Bofutrelvir far exceeds that to nirmatrelvir. This may be due to the fact that, in the complex with Bofutrelvir, although S144A exhibits minimal changes in side chain size and appears to only affect the hydrogen bond formed between the missing hydroxyl group and L141, the overall structure of the S144A and Bofutrelvir complex reveals severe disruption of hydrogen bond formation between F140 and the (S)-γ-lactone ring NH of Bofutrelvir, as well as the hydrogen bond formation between Glu166 and the NH of the P3 and P4 of Bofutrelvir (Figs. 3e and 4e). These hydrogen bonds are intact in the structure of S144A with nirmatrelvir (Fig. S5a, b)[27]. The disappearance of these hydrogen bonds is the reason why the resistance of the S144A mutant to Bofutrelvir far exceeds that to nirmatrelvir. Additionally, for nirmatrelvir, the the IC_{50} value for the E166R mutant is 3.712 μM, while the IC_{50} value for the E166N mutant is greater than 100 μM[25]. Additionally, the E166R mutant also shows an increased IC_{50} for other inhibitors, such as PF-0085231 and GC-376, compared to the wild-type M^pro[25].

The His163A mutation, which replaces histidine (H) with alanine (A), eliminates key hydrogen bond interactions with Bofutrelvir. Our structural studies revealed that the absence of histidine destabilizes the binding pocket, significantly weakening Bofutrelvir's efficacy. The His163A mutation greatly reduced the binding affinity and overall inhibitory potency of the inhibitor, causing substantial changes in the orientation of Bofutrelvir within the active site, including at the S1′, S1, and S2 subsites (Figs. 1c, 2f, and 3c). For enzyme activity, the H163A mutant exhibits significantly reduced catalytic activity, with a catalytic efficiency (k_{cat}) ~30-fold lower than that of the wild type[26]. The IC_{50} value of the H163A mutant may also reflect its decreased enzyme activity, potentially indicating further impact on its sensitivity to inhibitors. These findings highlight the critical role of His163 in maintaining the structural integrity of the binding pocket and the stability of the inhibitor, with mutations at these sites leading to significant reductions in both enzyme activity and increased resistance to inhibitors.

We also evaluated the inhibitory effects of Bofutrelvir on MERS-CoV M^pro. The results showed that the IC_{50} value of Bofutrelvir for MERS-CoV M^pro was 12.11 μM, significantly higher than the 0.021 μM for wild-type SARS-CoV-2 M^pro, indicating a reduction in efficacy by over 200-fold. This suggests that structural differences between MERS-CoV M^pro and SARS-CoV-2 M^pro severely impact the binding efficiency of Bofutrelvir. Our structural analysis indicated that the lack of hydrogen bonds at the S4 subsite is a key factor in the reduced inhibitory activity. MERS-CoV M^pro lacks the

critical hydrogen bond interactions with Bofutrelvir at E166 in SARS-CoV-2 M^pro, resulting in reduced stability and binding affinity of the inhibitor.

Through detailed structural analysis, we discovered significant changes in the geometric structure and hydrogen bond network of the binding pocket when Bofutrelvir binds to E166N, E166R, E166V, S144A, and His163A mutants. These mutations alter the binding mode of the inhibitor, resulting in a certain degree of reduced enzyme activity and impaired replication fitness, as well as leading to a substantial decrease in stability and affinity. Additionally, the lack of hydrogen bonds at the S4 subsite in MERS-CoV M^pro results in reduced stability of inhibitor binding, further explaining the significantly reduced inhibitory effect of Bofutrelvir. Our findings emphasize the importance of understanding the structural basis of viral protease mutations and their impact on drug resistance. The significant reduction in the inhibitory efficacy of Bofutrelvir against E166N, E166R, E166V, S144A, and His163A mutants, as well as MERS-CoV M^pro, highlights the challenges posed by viral mutations to the development of effective antiviral therapies. Besides, Cross-resistance is particularly evident in nirmatrelvir and ensitrelvir, which share a similar binding mode to Bofutrelvir, especially with regard to the E166V mutation. the inhibitors developed for SARS-CoV-2 M^pro, such as Enstrelvir and Nirmatrelvir (with a similar binding mode to Bofutrelvir), also exhibit significant cross-resistance with Bofutrelvir, with the E166V mutation playing a particularly significant role[27]. This phenomenon suggests that if inhibitors share similar binding sites and mechanisms, the SARS-CoV-2 can develop cross-resistance. However, Enstrelvir displays a relatively lower level of resistance, which may be attributed to its unique binding mode: compared to Bofutrelvir and Nirmatrelvir, Enstrelvir does not form direct hydrogen bonding with the E166 side chain and has weaker dependence on the S1 subsite[27]. This discovery hints that inhibitors with different binding mechanisms may be able to avoid the challenges posed by Bofutrelvir, Nirmatrelvir, and other similar inhibitors-resistant mutants. Therefore, to develop the next generation of M^pro inhibitors without cross-resistance, future research should focus on creating inhibitors that bind to the M^pro catalytic site in unique ways[27]. These inhibitors should avoid the subsite binding strategies employed by Bofutrelvir and instead target regions within the catalytic pocket that are not adequately occupied by existing drugs, thereby effectively inhibiting M^pro activity. Additionally, strategies such as non-covalent binding, allosteric inhibition, or covalent warhead optimization can be explored to reduce dependence on mutable residues like E166 and S144. These next-generation drugs may also cooperate with other therapeutic agents or inhibitors targeting different sites, enhancing antiviral efficacy through multi-pathway and delaying the emergence of resistance. This next generation of inhibitors not only addresses resistance issues arising from mutations such as E166V but also provides more durable clinical solutions for the treatment of COVID-19.

Methods
Construction and purification of of various M^pro
The gene encoding M^pro from MERS-CoV and SARS-CoV-2 were synthetically designed with codon optimization to enhance expression in *Escherichia coli* by Beijing Tsingke Biotech Co., Ltd, and these genes were subsequently cloned into the pET-28a vector using BamHI-XhoI restriction sites, incorporating an N-terminal 6 × His tag for purification purposes. The competent *E. coli* cells were purchased from TIANGEN Biotech (Beijing) Co., Ltd. Site-directed mutagenesis was utilized to produce the E166N, E166R, and H163A variants of SARS-CoV-2 M^pro, with these mutations confirmed by DNA sequencing. The recombinant plasmids were transformed into *E. coli* Rosetta DE3 cells to express the M^pro proteins. Following expression protocols established in our lab, the proteins were expressed and purified[32]. SARS-CoV-2 M^pro mutants and MERS-CoV M^pro were expressed in *E. coli* cultured in 800 mL LB medium at 37 °C. At OD_{600} = 0.8, 500 μmol/L IPTG was added for induction, followed by 5 h incubation at 30 °C. Cells were harvested by centrifugation (10,000 × *g*, 15 min, 4 °C), and the pellet was resuspended in Buffer (100 mmol/L Tris/HCl, pH 7.5, 300 mmol/L NaCl, 10 mmol/L imidazole, 5% glycerol) and lysed using a JNBIO 3000 plus. After centrifugation (30,000 × *g*, 30 min, 4 °C), the

supernatant was loaded onto a 5 mL Ni-NTA column (GE Healthcare). The column was washed with Buffer (100 mmol/L Tris/HCl, pH 7.5, 300 mmol/L NaCl, 50 mmol/L imidazole, 5% glycerol), and the His-tagged protein was eluted with Buffer (50 mmol/L Tris-HCl, pH 7.5, 300 mmol/L NaCl, 300 mmol/L imidazole). Further purification was performed using a Superdex 200 PG column (GE Healthcare), and the buffer was exchanged to Buffer (25 mmol/L HEPES, pH 7.5, 300 mmol/L NaCl, 2 mmol/L DTT, 5% glycerol). Target protein fractions were identified by SDS-PAGE, flash-frozen in liquid nitrogen, and stored at −80 ℃.

Inhibition assay for enzymatic activity
The inhibitory effects of Bofutrelvir on M^{pro} were tested using fluorescent donor-quencher pairs synthesized in-house. FRET-based assays were performed in 384-well microplates, with PF-07321332 as a positive control. Each condition was independently repeated three times. Bofutrelvir and PF-07321332 stock solutions (10 mM) were prepared in DMSO, then diluted, mixed with 200 nM M^{pro}, and incubated at room temperature for 30 min. The reaction buffer contained 50 mM Tris-HCl (pH 7.3), 150 mM sodium chloride, and 1 mM EDTA. After incubation, the FRET substrate was added to initiate the reaction. Control groups included buffer-only, DMSO-only, positive control, and test groups. Fluorescence signals (RLU) were measured and recorded, and inhibitory efficacy (%) was calculated relative to the DMSO control using GraphPad Prism (version 9.3).

Crystallization of M^{pro} and Bofutrelvir complexes
M^{pro} proteins from MERS-CoV and the SARS-CoV-2 mutants (E166N, E166R, H163A) were concentrated to 15 mg/mL. Bofutrelvir was added at a 3:1 molar ratio and incubated on ice for 2 h before crystallization. Crystallization was performed at 18 ℃ using the hanging drop vapor diffusion method, mixing equal volumes (200 nL) of protein and reservoir solutions. The MERS-CoV M^{pro}-Bofutrelvir complex crystallized in 0.1 M HEPES (pH 7.5) and 18% w/v PEG 10000. For the SARS-CoV-2 M^{pro} mutants (E166R, H163A) in complex with Bofutrelvir, the conditions were 0.2 M sodium sulfate and 24% w/v PEG 3350. For the SARS-CoV-2 M^{pro} mutant (E166N) in complex with Bofutrelvir, the conditions were 0.1 M Hepes pH 6.5, 10% isopropanol, 22% PEG3350. For the SARS-CoV-2 M^{pro} mutant (E166V and S144A) in complex with Bofutrelvir, the conditions were 0.1 M BICINE pH 8.5, 20% w/v PEG10000.

Data collection and structural refinement
Crystals were cryoprotected with 20% glycerol and frozen in liquid nitrogen. X-ray diffraction data were collected at 100 K using the BL02U1, BL10U2, and BL17UM beamlines at the Shanghai Synchrotron Radiation Facility[53,54]. Data were processed with the aquarium pipeline, results summarized in Table 1[55]. M^{pro}-Bofutrelvir complex structures were solved by molecular replacement using Phaser[56]. Atomic coordinates and thermal factors were refined using Phenix, with model adjustments made in Coot[57,58]. Final models were validated with MolProbity[59]. Structural refinement details are in Table 1, with figures generated using PyMOL[60].

Molecular dynamics simulations
MD simulations of seven M^{pro}-bofutrelvir systems (SARS-CoV-2-wild-type, its five mutants and MERS-CoV) were performed using Gromacs v2022.03 (100 ns each) with AMBER99SB-ILDN for M^{pro}s and GAFF for bofutrelvir[61–64]. Initial docked structures (pdb to gro format) were solvated in TIP3P water (1.2 nm buffer), neutralized with Na^+/Cl^c (0.154 M), and energy-minimized via steepest descent[65,66]. Bofutrelvir parameters were derived from Gaussian 16 W hydrogenation and RESP charges. Short-range interactions used 1.0 nm cutoffs, with PME for long-range electrostatics[67]. LINCS constrained hydrogen bonds[68]. Temperature control (300 K) utilized V-rescale, while pressure (1 atm) used Berendsen barostat[69,70]. Equilibration included: 100 ps solvent pre-equilibration, 100 ps NVT (300 K), and 100 ps NPT (1 atm). Based on the MD simulation trajectories, we analyzed the RMSD (root mean square deviation), RMSF (root mean square fluctuation),

and hydrogen bonds of the complexes. Additionally, the binding free energy of M^{pro} and its mutants with bofutrelvir was calculated using the MM/PBSA method[71].

Binding energy calculation
MM/PBSA calculation method systematically decomposes the molecular binding free energy (ΔG_{bind}) into three core components through thermodynamic partitioning: gas-phase molecular mechanics free energy (ΔG_{gas}), solvation free energy ($\Delta G_{solvation}$) and entropy term (ΔG_{TS}, also -TΔS). Among them, the gas-phase free energy is further decomposed into the synergistic contributions of van der Waals interaction energy (ΔG_{vew}) and electrostatic potential energy (ΔG_{elec}). Solvation free energy, is composed of polar solvation energy (ΔG_{EGB}, calculated using the Generalized Born model) and non-polar solvation energy (ΔG_{surf}, related to the solvent accessible surface area). The final binding free energy is expressed as the algebraic sum of ΔGgas, ΔG_{TS}, and ΔGsolvation, and its negative value directly represents the binding affinity of the ligand-protein complex[71].

Ethics and inclusion statement
This manuscript does not involve ethical issues as no relevant experiments were conducted. All data and materials presented are fully available and reproducible, ensuring transparency and reliability in our research.

Statistics and reproducibility
For the inhibition assay of M^{pro} activity, the experiments were carried out at least three times using separate protein batches to ensure reproducibility.

Reporting summary
Further information on research design is available in the Nature Portfolio Reporting Summary linked to this article.

Data availability
The atomic coordinates and structure factors for the MERS-CoV-M^{pro}-Bofutrelvir, SARS-CoV-2-M^{pro}(E166N)-Bofutrelvir, SARS-CoV-2-M^{pro}(E166R)-Bofutrelvir, SARS-CoV-2-M^{pro}(H163A)-Bofutrelvir, SARS-CoV-2-M^{pro}(E166V)-Bofutrelvir and SARS-CoV-2-M^{pro}(S144A)-Bofutrelvir complexes are available in the Protein Data Bank (https://www.rcsb.org/) with accession numbers 9INM, 8YWY, 9INL, 8YWZ, 9LUG and 9LUF. Source data are available with this paper. All uncropped and unedited gel images can be found in Supplementary (Fig. S6).

References
1. Zhong, N. S. et al. Epidemiology and cause of severe acute respiratory syndrome (SARS) in Guangdong, People's Republic of China, in February, 2003. *Lancet* **362**, 1353–1358 (2003).
2. Vijayanand, P., Wilkins, E. & Woodhead, M. Severe acute respiratory syndrome (SARS): a review. *Clin. Med.* **4**, 152–160 (2004).
3. Berger, A., Drosten, C., Doerr, H., Stürmer, M. & Preiser, W. Severe acute respiratory syndrome (SARS)—paradigm of an emerging viral infection. *J. Clin. Virol.* **29**, 13–22 (2004).
4. Abdel-Moneim, A.S. Middle East respiratory syndrome coronavirus (MERS-CoV): evidence and speculations. *Arch. Virol.* **159**, 1575–1584 (2014).
5. Fehr, A.R., Channappanavar, R. & Perlman, S. Middle east respiratory syndrome: emergence of a pathogenic human coronavirus. *Annu. Rev. Med.* **68**, 387–399 (2017).
6. Acter, T. et al. Evolution of severe acute respiratory syndrome coronavirus 2 (SARS-CoV-2) as coronavirus disease 2019 (COVID-19) pandemic: A global health emergency. *Sci. Total Environ.* **730**, 138996 (2020).
7. Lauxmann, M. A., Santucci, N. E. & Autrán-Gómez, A. M. The SARS-CoV-2 coronavirus and the COVID-19 outbreak. *Int. Braz. J. Urol.* **46**, 6–18 (2020).

8. Yu, Z. et al. Disruption in global supply chain and socio-economic shocks: a lesson from COVID-19 for sustainable production and consumption. *Oper. Manag. Res.* **15**, 233–248 (2022).

9. Clemente-Suárez, V. J. et al. The impact of the COVID-19 pandemic on social, health, and economy. *Sustainability* **13**, 6314 (2021).

10. Prescott, H.C. & Girard, T.D. Recovery from severe COVID-19: leveraging the lessons of survival from sepsis. *JAMA* **324**, 739–740 (2020).

11. Magwaza, N.N. et al. Mechanistic insights into targeting SARS-CoV-2 papain-like protease in the evolution and management of COVID-19. *BioChem* **4**, 268–299 (2024).

12. Liu, Y. et al. The development of Coronavirus 3C-Like protease (3CLpro) inhibitors from 2010 to 2020. *Eur. J. Med. Chem.* **206**, 112711 (2020).

13. Banerjee, R., Perera, L. & Tillekeratne, L. M. V. Potential SARS-CoV-2 main protease inhibitors. *Drug Discov. Today* **26**, 804–816 (2021).

14. Goyal, B. & Goyal, D. Targeting the dimerization of the main protease of coronaviruses: a potential broad-spectrum therapeutic strategy. *ACS Comb. Sci.* **22**, 297–305 (2020).

15. Anjum, F. et al. Identification of intrinsically disorder regions in non-structural proteins of SARS-CoV-2: New insights into drug and vaccine resistance. *Mol. Cell. Biochem.* **477**, 1607–1619 (2022).

16. Li, X. & Song, Y. Structure and function of SARS-CoV and SARS-CoV-2 main proteases and their inhibition: A comprehensive review. *Eur. J. Med. Chem.* **260**, 115772 (2023).

17. Kneller, D. W. et al. Structural plasticity of SARS-CoV-2 3CL Mpro active site cavity revealed by room temperature X-ray crystallography. *Nat. Commun.* **11**, 3202 (2020).

18. Zhang, Y. -Z. & Holmes, E. C. A genomic perspective on the origin and emergence of SARS-CoV-2. *Cell* **181**, 223–227 (2020).

19. Awoonor-Williams, E. & Abu-Saleh, A. A. Covalent and non-covalent binding free energy calculations for peptidomimetic inhibitors of SARS-CoV-2 main protease. *Phys. Chem. Chem. Phys.* **23**, 6746–6757 (2021).

20. Liu, Y., Ming, W., Li, C.-Z., Zhu, Y.-Y. & Gu, S.-X. Advances in peptidomimetic inhibitors of coronavirus main protease. *Acta Pharm. Sin.* **57**, 1977–1990 (2022).

21. Shang, W. et al. In vitro and in vivo evaluation of the main protease inhibitor FB2001 against SARS-CoV-2. *Antivir. Res.* **208**, 105450 (2022).

22. Dai, W. et al. Structure-based design of antiviral drug candidates targeting the SARS-CoV-2 main protease. *Science* **368**, 1331–1335 (2020).

23. Hu, Y. et al. Naturally occurring mutations of SARS-CoV-2 main protease confer drug resistance to nirmatrelvir. *ACS Cent. Sci.* **9**, 1658–1669 (2023).

24. Mótyán, J. A., Mahdi, M., Hoffka, G. & Tőzsér, J. Potential resistance of SARS-CoV-2 main protease (Mpro) against protease inhibitors: lessons learned from HIV-1 protease. *Int. J. Mol. Sci.* **23**, 3507 (2022).

25. Ou, J. et al. A yeast-based system to study SARS-CoV-2 Mpro structure and to identify nirmatrelvir resistant mutations. *PLoS Pathog.* **19**, e1011592 (2023).

26. Tran, N. et al. The H163A mutation unravels an oxidized conformation of the SARS-CoV-2 main protease. *Nat. Commun.* **14**, 5625 (2023).

27. Duan, Y. et al. Molecular mechanisms of SARS-CoV-2 resistance to nirmatrelvir. *Nature* **622**, 376–382 (2023).

28. Iketani, S. et al. Multiple pathways for SARS-CoV-2 resistance to nirmatrelvir. *Nature* **613**, 558–564 (2023).

29. Zhu, Y. et al. In vitro selection and analysis of SARS-CoV-2 nirmatrelvir resistance mutations contributing to clinical virus resistance surveillance. *Sci. Adv.* **10**, eadl4013 (2024).

30. Huang, C. et al. A new generation Mpro inhibitor with potent activity against SARS-CoV-2 Omicron variants. *Signal Transduct. Target. Ther.* **8**, 128 (2023).

31. Nakayoshi, T., Kato, K., Kurimoto, E. & Oda, A. Virtual alanine scan of the main protease active site in severe acute respiratory syndrome coronavirus 2. *Int. J. Mol. Sci.* **22**, 9837 (2021).

32. Li, J. et al. Crystal structure of SARS-CoV-2 main protease in complex with the natural product inhibitor shikonin illuminates a unique binding mode. *Sci. Bull.* **66**, 661–663 (2021).

33. Wang, W. -w. et al. Structural Basis of Main Proteases of Coronavirus Bound to Bofutrelvir. *J. Mol. Biol.* **436**, 168784 (2024).

34. Machhi, J. et al. The natural history, pathobiology, and clinical manifestations of SARS-CoV-2 infections. *J. Neuroimmune Pharmacol.* **15**, 359–386 (2020).

35. Janik, E., Bartos, M., Niemcewicz, M., Gorniak, L. & Bijak, M. SARS-CoV-2: outline, prevention, and decontamination. *Pathogens* **10**, 114 (2021).

36. Ullrich, S. & Nitsche, C. The SARS-CoV-2 main protease as drug target. *Bioorg. Med. Chem. Lett.* **30**, 127377 (2020).

37. Zhang, L. et al. Crystal structure of SARS-CoV-2 main protease provides a basis for design of improved α-ketoamide inhibitors. *Science* **368**, 409–412 (2020).

38. Padhi, A. K. & Tripathi, T. Hotspot residues and resistance mutations in the nirmatrelvir-binding site of SARS-CoV-2 main protease: Design, identification, and correlation with globally circulating viral genomes. *Biochem. Biophys. Res. Commun.* **629**, 54–60 (2022).

39. Jochmans, D. et al. The substitutions L50F, E166A, and L167F in SARS-CoV-2 3CLpro are selected by a protease inhibitor in vitro and confer resistance to nirmatrelvir. *MBio* **14**, e02815–e02822 (2023).

40. Zhou, Y. et al. Nirmatrelvir-resistant SARS-CoV-2 variants with high fitness in an infectious cell culture system. *Sci. Adv.* **8**, eadd7197 (2022).

41. Shaqra, A. M. et al. Defining the substrate envelope of SARS-CoV-2 main protease to predict and avoid drug resistance. *Nat. Commun.* **13**, 3556 (2022).

42. Al Adem, K., Ferreira, J. C., Fadl, S., Mustafa, M. & Rabeh, W. M. Key allosteric and active site residues of SARS-CoV-2 3CLpro are promising drug targets. *Biochem. J.* **480**, 791–813 (2023).

43. Weng, Y. L. et al. Molecular dynamics and in silico mutagenesis on the reversible inhibitor-bound SARS-CoV-2 main protease complexes reveal the role of lateral pocket in enhancing the ligand affinity. *Sci. Rep.* **11**, 7429 (2021).

44. Shitrit, A. et al. Conserved interactions required for inhibition of the main protease of severe acute respiratory syndrome coronavirus 2 (SARS-CoV-2). *Sci. Rep.* **10**, 20808 (2020).

45. Krismer, L. et al. Study of key residues in MERS-CoV and SARS-CoV-2 main proteases for resistance against clinically applied inhibitors nirmatrelvir and ensitrelvir. *npj Viruses* **2**, 23 (2024).

46. Tan, J. et al. pH-dependent conformational flexibility of the SARS-CoV main proteinase (Mpro) dimer: molecular dynamics simulations and multiple X-ray structure analyses. *J. Mol. Biol.* **354**, 25–40 (2005).

47. Hilgenfeld, R. et al. in *The Nidoviruses* (eds Stanley, P. & Kathryn, V. H.) 581, 585–591 (Springer US, 2006).

48. Shi, Y. et al. The preclinical inhibitor GS441524 in combination with GC376 efficaciously inhibited the proliferation of SARS-CoV-2 in the mouse respiratory tract. *Emerg. Microbes Infect.* **10**, 481–492 (2021).

49. Zhang, Y. et al. Structure-based discovery and structural basis of a novel broad-spectrum natural product against the main protease of coronavirus. *J. Virol.* **96**, e01253–01221 (2022).

50. Owen, D. R. et al. An oral SARS-CoV-2 Mpro inhibitor clinical candidate for the treatment of COVID-19. *Science* **374**, 1586–1593 (2021).

51. Hammond, J. et al. Oral nirmatrelvir for high-risk, nonhospitalized adults with Covid-19. *N. Engl. J. Med.* **386**, 1397–1408 (2022).

52. Zhao, Y. et al. Crystal structure of SARS-CoV-2 main protease in complex with protease inhibitor PF-07321332. *Protein Cell* **13**, 689–693 (2022).

53. Liu, K. et al. BL02U1: the relocated macromolecular crystallography beamline at the Shanghai Synchrotron Radiation Facility. *Nucl. Sci. Tech.* **34**, 193 (2023).

54. Xu, Q. et al. The biosafety level-2 macromolecular crystallography beamline (BL10U2) at the Shanghai Synchrotron Radiation Facility. *Nucl. Sci. Tech.* **34**, 202 (2023).

55. Yu, F. et al. Aquarium: an automatic data-processing and experiment information management system for biological macromolecular crystallography beamlines. *J. Appl. Crystallogr.* **52**, 472–477 (2019).

56. McCoy, A. J. et al. Phaser crystallographic software. *J. Appl. Crystallogr.* **40**, 658–674 (2007).

57. Adams, P. D. et al. PHENIX: a comprehensive Python-based system for macromolecular structure solution. *Acta Crystallogr. Sect. D.* **66**, 213–221 (2010).

58. Emsley, P., Lohkamp, B., Scott, W. G. & Cowtan, K. Features and development of Coot. *Acta Crystallogr. Sect. D.* **66**, 486–501 (2010).

59. Chen, V. B. et al. MolProbity: all-atom structure validation for macromolecular crystallography. *Acta Crystallogr. Sect. D.* **66**, 12–21 (2010).

60. DeLano, W. L. The PyMOL molecular graphics system. http://www.pymol.org/ (2002).

61. Van Der Spoel, D. et al. GROMACS: fast, flexible, and free. *J. Comput. Chem.* **26**, 1701–1718 (2005).

62. Abraham, M. J. et al. GROMACS: High performance molecular simulations through multi-level parallelism from laptops to supercomputers. *SoftwareX***1-2**, 19–25 (2015).

63. Lindorff-Larsen, K. et al. Improved side-chain torsion potentials for the Amber ff99SB protein force field. *Proteins* **78**, 1950–1958 (2010).

64. Özpınar, G. A., Peukert, W. & Clark, T. An improved generalized AMBER force field (GAFF) for urea. *J. Mol. Model.* **16**, 1427–1440 (2010).

65. Nayar, D., Agarwal, M. & Chakravarty, C. Comparison of tetrahedral order, liquid state anomalies, and hydration behavior of mTIP3P and TIP4P water models. *J. Chem. Theory Comput.* **7**, 3354–3367 (2011).

66. Donnelly, S. M., Lopez, N. A. & Dodin, I.Y. Steepest-descent algorithm for simulating plasma-wave caustics via metaplectic geometrical optics. *Phys. Rev. E* **104**, 025304 (2021).

67. Essmann, U. et al. A smooth particle mesh Ewald method. *J. Chem. Phys.* **103**, 8577–8593 (1995).

68. Hess, B., Bekker, H., Berendsen, H. J. C. & Fraaije, J. G. E. M. LINCS: A linear constraint solver for molecular simulations. *J. Comput. Chem.* **18**, 1463–1472 (1997).

69. Berendsen, H. J. C., Postma, J. P. M., Gunsteren, W. F. V., Dinola, A. & Haak, J. R. Molecular dynamics with coupling to an external bath. *J. Chem. Phys.* **81**, 3684–3690 (1984).

70. Bou-Rabee, N. Time Integrators for Molecular Dynamics. *Entropy* **16**, 138–162 (2014).

71. Genheden, S. & Ryde, U. The MM/PBSA and MM/GBSA methods to estimate ligand-binding affinities. *Expert Opin. drug Discov.* **10**, 449–461 (2015).

Acknowledgements

Author contributions

Wei-wei Wang: investigation, formal analysis, Writing—original draft. Xue-lan Zhou: investigation, formal analysis, Writing—original draft. Wen-wen Li: formal analysis, investigation. Pei Zeng: formal analysis, investigation. Li Guo: formal analysis, investigation. Qisheng Wang: conceptualization, supervision, Writing—review and editing, project administration. Jian Li: conceptualization, supervision, Writing—review and editing, project administration. All authors have read and agreed to the published version of the manuscript.

Competing interests

The authors declare no competing interests.

Additional information

Supplementary information The online version contains supplementary material available at https://doi.org/10.1038/s42003-025-07929-9.

Correspondence and requests for materials should be addressed to Qisheng Wang or Jian Li.

Peer review information *Communications Biology* thanks the anonymous reviewers for their contribution to the peer review of this work. Primary Handling Editors: Tuan Anh Nguyen and Laura Rodríguez Pérez. [A peer review file is available].

Reprints and permissions information is available at http://www.nature.com/reprints

Publisher's note Springer Nature remains neutral with regard to jurisdictional claims in published maps and institutional affiliations.